Journal of Nuclear Materials 377 (2008) 313–324

Contents lists available at ScienceDirect

Journal of Nuclear Materials

journal homepage: www.elsevier.com/locate/jnucmat

Fission product release and microstructure changes during laboratory annealing of a very high burn-up fuel specimen

J.-P. Hiernaut [a,*], T. Wiss [a], J.-Y. Colle [a], H. Thiele [a], C.T. Walker [a], W. Goll [b], R.J.M. Konings [a]

[a] European Commission Joint Research Centre, Institute for Transuranium Elements, P.O. Box 2340, 76125 Karlsruhe, Germany
[b] AREVA NP GmbH, Freyerslebenstr., 1 D-91058 Erlangen, Germany

ARTICLE INFO

Article history:
Received 8 January 2008
Accepted 3 March 2008

ABSTRACT

A commercial PWR fuel sample with a local burn-up of about 240 MWd/kgHM was annealed in a Knudsen cell mass spectrometer system with a heating rate of 10 K/min up to 2750 K at which temperature the sample was completely vaporized. The release of fission gases and fission products was studied as a function of temperature. In one of the runs the heating was interrupted successively at 900, 1500 and 1860 K and at each step a small fragment of the sample was examined by SEM and analysed by energy dispersive electron probe microanalysis. The release behaviour of volatile, gaseous and other less volatile fission products is presented and analysed with the EFFUS program and related to the structural changes of the fuel.

1. Introduction

Extension of the authorised burn-up of LWR fuel is an important issue for nuclear reactor operation. The benefits of increased fuel burn-up are a decrease in the volume of spent fuel discharged and fuel cycles cost. It also leads to less refuelling operations and thus higher availability. With the increase of the burn-up, it has become important to establish the practical limitations that may arise from the physical evolution of the fuel.

A possible limitation could be the restructuring of the UO_2 fuel that occurs at the pellet periphery in high burn-up LWR fuel. This restructuring was observed for the first time in very high burn-up fuel in the late 1950s as described by Belle [1]. It is generally called the high-burn-up structure (HBS) or rim structure. This structure starts to form when the local burn-up exceeds about 60 MWd/kgHM. The formation of the HBS is characterised by four consecutive phases: nucleation of re-crystallised grains at grain boundaries and pores, loss of xenon from the new grain structure, formation of micrometer size pores in the re-crystallized new structure as a result of diffusion of fission gas out of the new grain structure, growth of the new pores with increase in the local burn-up as they collect the gas that continuously flow from the surrounding re-crystallised grains.

The HBS has been extensively investigated for almost 20 years and many properties and characteristics of this structure have been measured, including microstructure changes, fission gas release and xenon depletion, porosity, thermal conductivity, oxidation state, and lattice parameter [2–9]. But there is still some discussion about the formation processes [10–12].

Little information exists about the evolution of the HBS and the release of fission gas and fission products as a function of temperature, except measurements done in the frame of the HBRP-Rim project [13,14] on constrain free UO_2 samples irradiated at different burn-up ranging from 30 to 96 MWd/kgHM. The thermal conductivity evolution versus the burn-up has been published [15] but the fission gas release measured during thermal annealing has been only partly published.

In this paper we present the evolution of the microstructure and the fission gas and fission products release observed during thermal annealing of a fuel sample coming from a region close to the fuel rim in a commercial PWR fuel with an average burn-up of 98 MWd/KgHM. These observations and measurements could contribute to a better understanding of the HBS formation mechanisms and the behaviour of the fission products in the HBS. In the open literature there is no real indication of the total gas quantity remaining in the fuel and no real consensus on gas behaviour at such high burn-up. Therefore, a tentative quantification of the fission gas in this sample is made comparing results obtained on different UO_2 and MOX fuels with the calculated values.

2. Fuel samples

The samples were small pieces of 4 and 6 μg originating from the periphery ($0.91 < r/r_o < 1$) of a fuel pellet of average burn-up 102 MWd/kgHM. The radial width of the samples was ~800 μm. A microscopic image of the sample as obtained by SEM is shown in Fig. 1. The area of the sample close to the pellet periphery ($Z_a \approx 1/3$ of the sample) shows larger pores of ~4 μm in diameter with the typical 'cauliflower' structure of the HBS visible inside. In the other parts ($Z_b \approx 2/3$ of the sample) pores of ~2 μm are homogeneously distributed. The grain size in the sample is ranging

* Corresponding author. Tel.: +49 7247 951 385; fax: +49 7247 951 99385.
E-mail address: Jean-Pol.Hiernaut@ec.europa.eu (J.-P. Hiernaut).

0022-3115/$ - see front matter © 2008 Elsevier B.V. All rights reserved.
doi:10.1016/j.jnucmat.2008.03.006

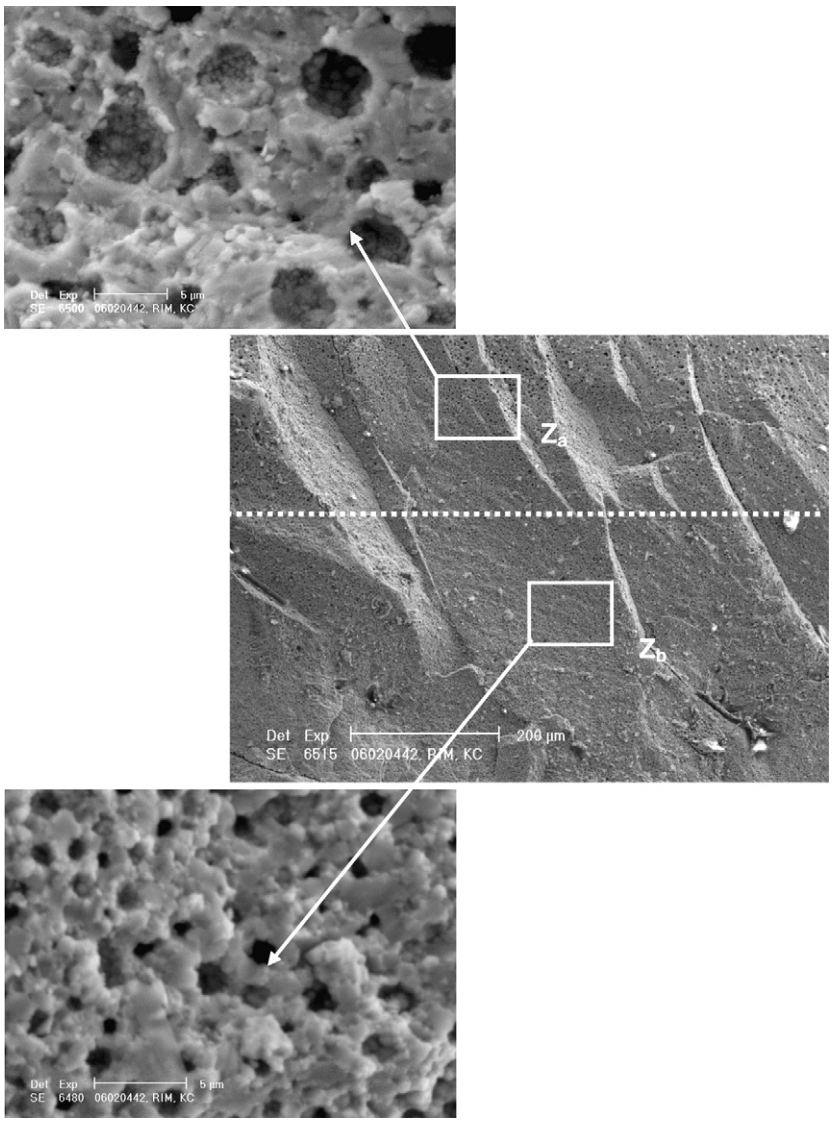

Fig. 1. Secondary electron images showing an overview of the microscopic structure of the UO_2 rim sample. A dashed line delimits two regions: a region near the periphery (Z_a) and a region some micron further in (Z_b). The gas pores are noticeably larger in region Z_a.

from 0.2 to 0.5 μm. The maximum local burn-up of these samples is about 240 MWd/kgHM at the outer rim and about 160 MWd/kgHM at the inner side, the estimated average being (200 ± 20) MWd/kgHM. The characteristics and the irradiation history of the fuel have been described in [9].

By tilting the sample to the secondary electron detector in the microscope, a pattern was observed that suggested a memory effect of the initial grain structure of the un-irradiated material (Fig. 2). The surface examined is a fractured surface and the secondary electron micrograph reveals the original grain boundaries through localized charging effects. The peculiar charging at the location of the original grain boundaries is attributed to the preferential precipitation and accumulation of fission products causing a local embrittlement. The sharp inter-granular fractures along these original grain boundaries collect a charge from the electron beam providing the distinct contrast visible in Fig. 2.

3. Experimental method

A tungsten Knudsen cell combined with a quadrupole mass spectrometer (KCMS) was used to measure the release of fission gases and fission products. The Knudsen cell was heated by a high temperature induction furnace and the temperature was measured by a pyrometer. The ionisation energy (E) was kept constant at 40 eV. This energy is sufficient to ionise all species, but is too high to avoid dissociation of molecules. The technique and the system have been described earlier [16–18].

The system is calibrated by placing a known quantity of silver in the Knudsen cell together with the sample (no reaction occurs since silver is totally vaporised at 1500 K, before matrix evaporation starts effectively). From the ion intensities (I_{Ag}) of the silver isotopes ^{107}Ag and ^{109}Ag, and the vapour pressure of silver (p_{Ag}) from the open literature [19] a global calibration factor of silver (K_{Ag}) can be derived using Eq. (I).

$$p_{Ag} = I_{Ag} T_{Ag} K_{Ag} \tag{I}$$

Taking into account the ionisation cross-sections (σ) [20,21] and the appearance potentials (AP) of Ag and the element i measured, it is possible to determine the partial vapour pressure of any vaporising species (i) from their ion signals (I_i).

$$p_i = I_i T_i K_{Ag} M_i^{1/2} C_i \tag{II}$$

where

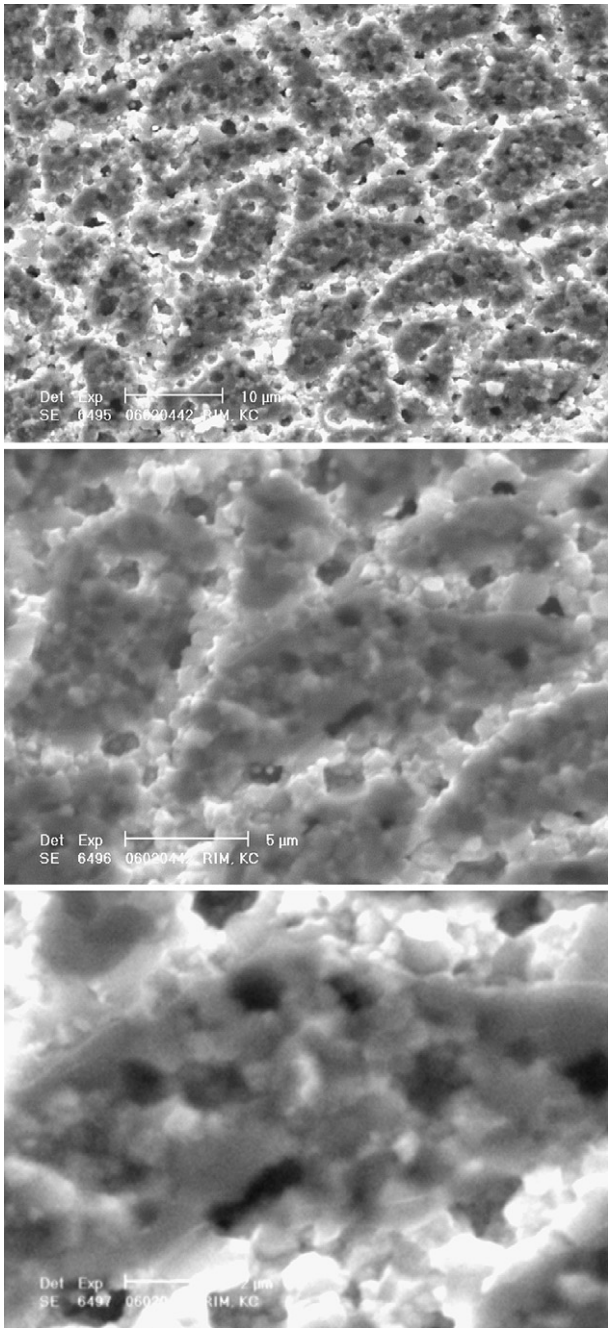

Fig. 2. SEM micrographs at different magnifications showing a 'memory effect' of the original grain structure in the high burn-up structure of the rim sample. The contours of the original grains are clearly visible as a network of bright lines along the former grain boundaries.

$$C_i = \sigma_{Ag}(E_{Ag} - AP_{Ag})/(M_{Ag}^{1/2}\sigma_i - AP_i) \quad \text{(III)}$$

Under Knudsen-effusion conditions, the vapour pressure of species i at temperature T,is proportional to the mass effused during the time $t(G_i)$ [22]

$$P_i = [G_i/(CS_{or}t)](2\pi RT/M_i)^{1/2} \quad \text{(IV)}$$

where C is the Clausing factor (is normally included in K_i), S_{or} the area of the Knudsen cell orifice, R the universal gas constant, and M_i the mass of the species.

The quantity of every species effusing trough the cell orifice per unit time, G_i, is given by Eq. (V). The total quantity is obtained by cycle summation of $G_i(\Delta t)$.

$$\sum Gi = [1/(2\pi R)^{1/2}]\sum(I_i T^{1/2}\Delta t K M_i C_i S_{or}) \quad \text{(V)}$$

where Δt is the length of a cycle in s, and K the calibration factor with silver as reference. The latter is not usable for quantification of gas but enough to determine the ratio of signals.

In order to quantify the fission gas present in the sample, the gas released during thermal annealing was condensed at the outlet of the pumping system, in a liquid nitrogen trap filled with active carbon. The system is equipped with a calibrated gamma counter to measure the ^{85}Kr activity. After warming up the trap, the liberated gas was compressed into a container and spiked with different isotopes of the various elements and measured quantitatively by a mass spectrometer technique (QGAMES). The correct ratio of signals to measure the isotopic composition or abundance ratio of fission gas can be determined from the ratio of $\int G_i dt$.

Two experiments were performed:

- The first sample of 6 mg was heated at a rate of 30 K/min from room temperature to 2750 K. At this temperature vaporization was complete. All the masses between 83 and 300 were measured. ^{85}Kr was also detected by a β-counter.
- The second sample (4 mg) was heated stepwise at a rate of 10 K/min to 900, 1500, and 1850 K. Only He and the volatile fission products were measured during this annealing. After each step a fragment of the sample was removed for scanning electron microscopy (SEM) microstructural examination and energy dispersive X-ray (EDX) analysis. The instrument used in the study was a SEM XL40 from Philips modified to allow the examination of radioactive samples. The electron column with turbo-molecular pump and EDX detector has been mounted in a glove-box.
- The release curves of the fission products were analysed using the EFFUS program. [16,18,23].
- The different heating rate between the two experiments did not influence markedly the release results.

4. Fission product release

4.1. Fission gases and volatile fission products

The release of fission gases is shown in Fig. 3 together with UO_2 vapour species and the volatile fission products in Fig. 4. For all elements the release curves of the different isotopes were similar, except in case of interferences i.e. $^{85}Kr^+$ and $^{85}Rb^+$, and at high

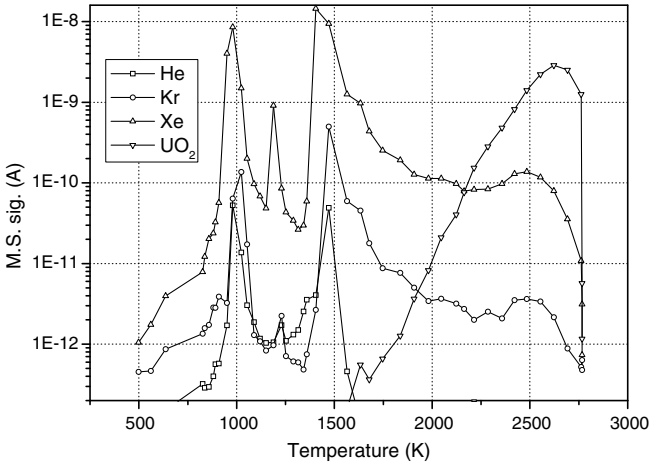

Fig. 3. Measured release of He and the fission gases Kr and Xe. The vaporization curve of UO_2 is shown for comparison.

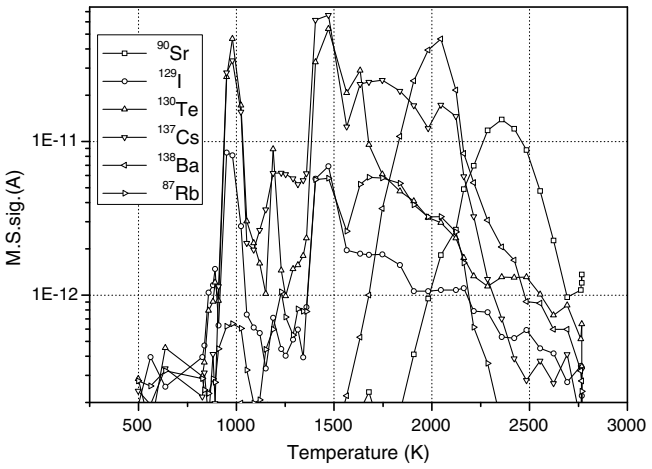

Fig. 4. Measured release of the volatile fission products Rb, I, Te, Cs and less volatilefission products: Ba, Sr.

temperature for $^{135}Cs^{+}$ and $^{238}UO_2^{2+}$. For clarity in the graphs, only one representative isotope is reported.

Helium release takes place in three steps. The first, occurring between 600 and 800 K is attributed to helium released from the grain boundaries and corresponds to ~1% of the inventory. The second occurs between 900 and 1000 K and corresponds to about 35% of the inventory. The third step occurs between 1400 and 1500 K and concerns the remaining 64% of the inventory. No helium was detected at higher temperatures, excluding re-precipitation mechanisms.

The fission gases Kr and Xe present almost identical release curves composed of four steps: release of ~1% of the inventory in the first, between 600 and 800 K; 20% in the second between 900 and 1000 K; 70% in the third, between 1400 and 1500 K and the rest at higher temperature. It is assumed that the gas released in the last step is the re-precipitated fraction.

The volatile fission products I, Te, Cs and Rb also exhibit release in four steps. The three first steps are very similar to those for fission gases from the point of view of the temperature ranges, the second step representing 10–30% increasing from Cs to I. The fourth release step beginning at 1400 and finishing at 2100 for Cs and 2500 K for I involves a larger fraction of the inventory of these elements: 60% for Cs Rb and I, and 30% for Te. Barium and strontium exhibit smooth release curves having a single maximum at 2000 K and 2300 K, respectively. Strontium is detected in the vapour phase as $Sr^{+}$and no SrO^{+} was observed. Barium was detected as Ba^{+} and BaO^{+}. Both elements were completely released before full vaporization of the sample. The solubility of barium is very limited in UO_2 and grey phase precipitates ($Ba(U, Pu, Zr)O_3$ [24]) have been observed at 1800 K, as shown in Fig. 5.

Uranium dioxide vaporises smoothly during the annealing, and begins to be detectable above 1800 K. The vaporisation curve is given for comparison, to emphasise the fact that the larger part of the volatile fission products is released before vaporisation occurs (Ba and Sr are less volatile fission products). The vaporisation of the bulk (uranium oxide + lanthanides + actinides) will be the subject of another paper.

In addition to the release curves of the gases the evolution of the vacuum signal should be discussed. Parallel to the mass spectrometer measurements the vacuum signal was recorded every second. In contrast to the relatively smooth signals recorded by the mass spectrometer or with the β-counter, over a longer time interval the vacuum signal presents many more peaks or burst variations (Fig. 6). Superposed on the continuous release curve are release bursts which are interpreted by SEM observations of samples, annealed successively at 900, 1500 and 1800 K (see Section 5).

4.2. Fission gas quantification

The ratio Xe/Kr has been determined from $\int_t G_{Xe}dt/\int_t G_{Kr}dt$ measured in the Knudsen cell mass spectrometer system. The measurements done by Q-GAMES were only indicative, because no

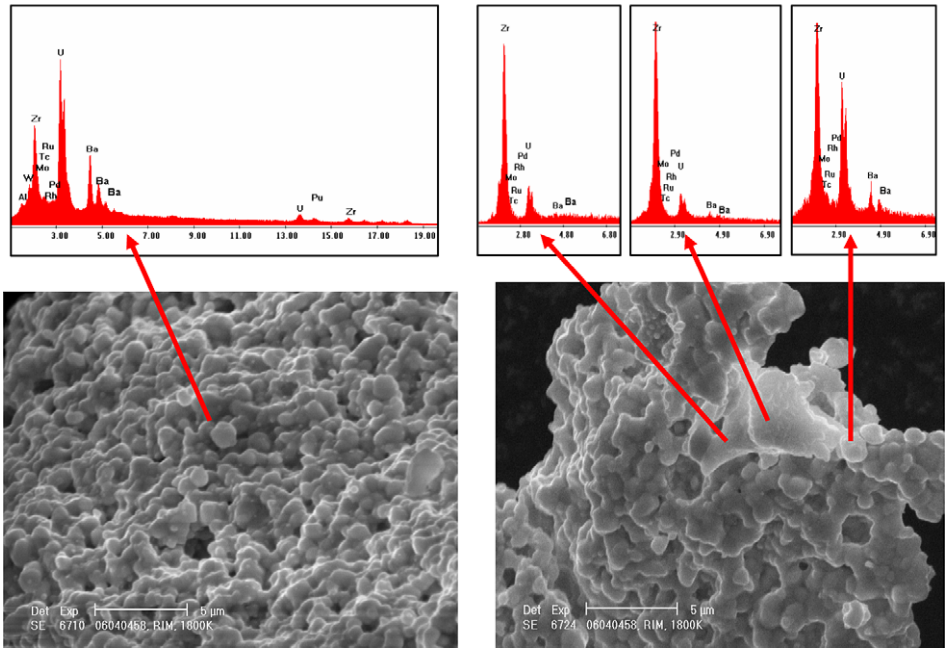

Fig. 5. SEM micrographs and EDX spectra showing Ba and Zr containing phases in the rim sample annealed at 1800 K.

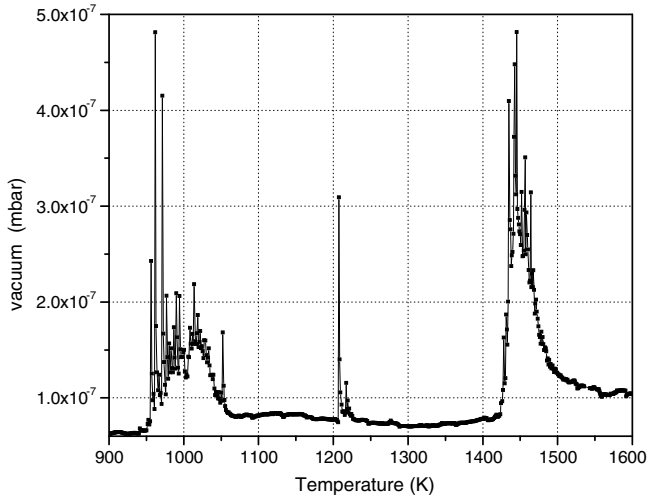

Fig. 6. Evolution of the vacuum (mbar) in the mass spectrometer chamber recorded during annealing of the sample and revealing burst release of volatile and/or gaseous products.

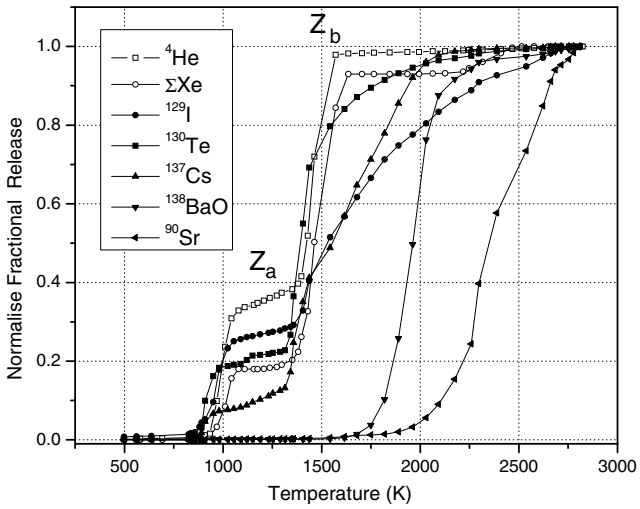

Fig. 7. Normalised fractional release of He, Xe, I, Te, Cs, BaO and Sr as a function of the annealing temperature.

stable xenon signals were obtained. The results are given in Table 1. The measured mass ratio Xe/Kr is equal to (53 ± 7) for a burn-up of (200 ± 20) MWd/kgHM, the molar ratio is (33.4 ± 7).

The quantity of ^{85}Kr was measured by γ-counting of the gas condensed in a liquid nitrogen trap. The total quantity of Kr has been obtained by the Q-GAMES method. The quantity of Xe was derived from the quantity of Kr multiplied by the ratio Xe/Kr. The results are given in Table 1. The total quantity of ^{85}Kr, Kr and Xe are respectively 1.13×10^{-6}, 1.02×10^{-5} and 3.41×10^{-4} mol/g (fuel). The quantity of He evaluated from the mass spectrometric signal, (G_{He} can not be used because the calibration factor of He cannot be deduce from the silver calibration), is 6.5×10^{-6} mol/g. The uncertainty of these values is estimated to be ±50%. It means that the quantity of Xe in the fuel is (4.5 ± 2.3) wt%.

4.3. Analysis of the release curves

The fractional release curves of gaseous and volatile fission products are shown in Fig. 7. They have been analysed with the program EFFUS, [16,18,25]. The results of the analysis are given in Table 2.

The activation energies of stages I and II obtained for He, Kr and Xe are in good agreement with previous work [18,23,25]. The mechanisms involved are: diffusion of gas in the bulk or re-dissolution and diffusion of the gas trapped in pores. The explosive release of gas due to lost of integrity of the sample has been smoothed; it represents only a small fraction of the gas inventory. The decreasing trend of the diffusion enthalpy of Xe in UO_2 with increase in the burn up seems to stabilise around 320 kJ/mol [25].

For Cs (Rb), I and Te, a well-marked stage I with low activation energy is observed at 980 K. This concerns about 10–30% of the inventory. As deduced from the microscopy observations, (Fig. 8) these fission products seem to form an amorphous-like phase around the pores. The activation energies of stage II are similar to previous results for a lower burn up fuel [25], but the activation energies of stage III are slightly lower. For Ba and Sr only the stage III has been detected with maxima successively at 2000 and 2300 K. The activation energies were confirmed also from an Arrhenius plot: $ln(p)$ versus $1/T$. The activation energy of 352 kJ/mol for Ba/BaO and 321 kJ/mol for Sr are very close despite the fact that the behaviour of these two fission products is very different: Sr is highly soluble as oxide in the UO_2 lattice, Ba is almost insoluble and is a major component of the 'grey phase' precipitates (Fig. 4). The grey phase precipitates have been detected at 1800 K and Ba is totally vaporised at 2300 K in agreement with [26].

Table 1
Ratio Xe/ Kr measured with Q-GAMES and the KCMS; quantity of ^{85}Kr, Kr and Xe measured successively by γ-counting, Q-Games and assessed from the Xe/Kr ratio

	Q-GAMES	γ-counting	KCMS	Assessed
Xe/Kr	> 15		33.4	33.4
^{85}Kr [mol/g]		1.13×10^{-6}		
Kr [mol/g]	1.02×10^{-5}			1.0×10^{-5}
Xe [mol/g]	$>2.7 \times 10^{-4}$			3.54×10^{-4}

5. Structural evolution of the fuel as a function of temperature

5.1. Microstructure

The grain size of the sample, is found to be constant (Fig. 1). The pores have a mean diameter of 4 μm in one third of the sample ($0.96 < r/r_o < 1$) that we indicate by Z_a and have a diameter of ~2 μm in the rest of the sample, Z_b ($0.91 < r/r_o < 0.96$). The annealing of the sample was done in three steps, after which the sample was examined by SEM. The following observations were made:

300–920 K: The sample was fractured after heating. Z_b broke in 2–3 big pieces of ~200 × 300 μm and Z_a in many small pieces of 10–30 μm. Fig. 9 shows the structure of these pieces at two magnifications. The grain dimensions remain 0.2–0.5 μm, the pores remain as they were in Z_a (Ø = 4 μm) and Z_b (Ø = 2 μm).

300–1500 K: At 1500 K, the sample has been entirely pulverized. The general and microscopic aspects are shown in Fig. 10, as well as a statistic counting of the powder pieces. Most of the pieces were small, between 10 and 20 μm and completely restructured. Also a clear re-sintering of the grains and an interconnection between the pores can be observed.

300 to 1800 K: The sintering of the grains is more pronounced at 1800 K as can be observed in Fig. 11. The grain size is about 1–5 μm and the pores are completely interconnected or agglomerated, metallic precipitates are visible.

Table 2
Release steps, temperature of maxima, yields (in relative units) and process enthalpies (diffusion, sublimation-vaporisation) obtained from EFFUS calculations, (fit of the normalised fractional release) for He, Kr, Xe, Cs, I, and from the slope of Arrhenius plot (ln*P* versus 1/*T*) for Ba and Sr

Species	T_{max} (K)	ΔH_I (kJ) *Yield*	T_{max} (K)	ΔH_{II} (kJ) *Yield*	T_{max} (K)	ΔH_{III} (kJ) *Yield*	Fit precision (%)
He	980	279.3 ± 3.6 *0.4*	1400	291.5 ± 3.1 *0.6*	–		1.3
Xe	980	291.7 ± 3.9 *0.2*	1400	339.0 ± 1.1 *0.75*	–	98 ± 32 *0.05*	1.6
Kr	980	289.5 ± 4.3 *0.2*	1400	341.1 ± 1.6 *0.75*	–	272.5 ± 30 *0.05*	1.6
Cs	980	84 ± 7.5 *0.1*	1400	392.7 ± 3.9 *0.4*	–	249.6 ± 7.5 *0.5*	1.7
I	–	104 ± 2.5 *0.3*	1400	361 ± 3.2 *0.1*	–	370 ± 1.6 *0.6*	1.61
Te	–	268.7 ± 7.5 *0.2*	1400	362 ± 2.6 *0.5*	–	368.9 ± 4.9 *0.3*	3.4
Ba	–	–	–	–	2000	352 ± .1.3 *1.0*	3.4
BaO	–	–	–	–	2000	354 ± 2.8 *1.0*	2.8
Sr	–	–	–	–	2300	321 ± 4.6 *1.0*	2.1

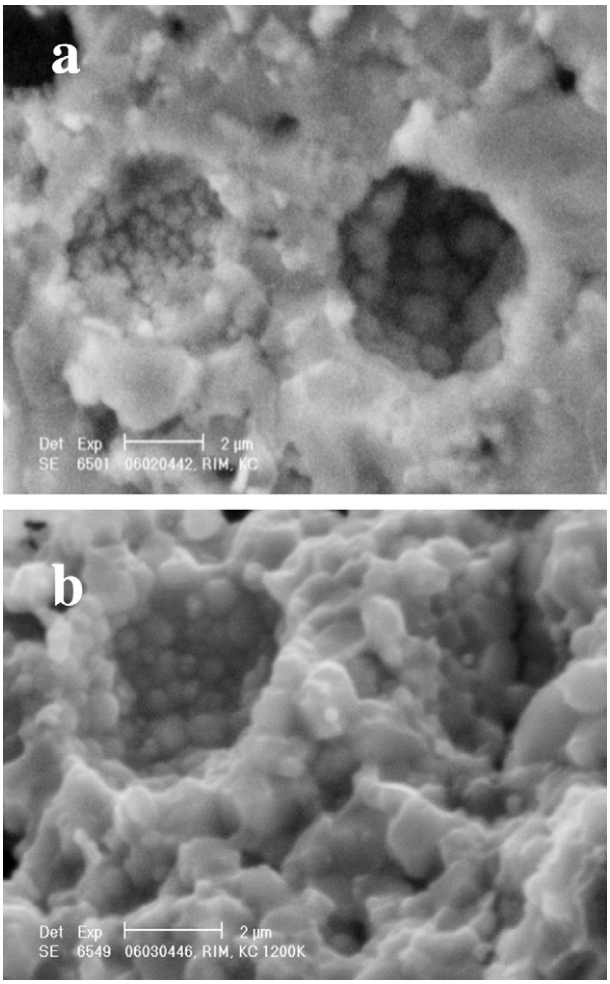

Fig. 8. SEM micrographs showing pores in zone Z_a where the burn-up is >200 MWd/KgHM, before (a) and after (b) annealing at 920 K.

5.2. Pore morphology

In the highest burn-up region different pore types were detected, as shown in Fig. 12. Among these pores, one type caught our attention (⩽1% of population), named hereafter 'ultimate pore'. It is perfectly round, and is surrounded by a vitreous-like phase mainly constituted of (U, Pu)O_x. It looks to be the end state of pores at very high burn-up. The non-thermal transformation of pores under very high irradiation leads to the formation of the so-called ultimate pore. Some steps of this process are depicted in Fig. 13. The transformation probably originated from sputtering of the material constituting the wall of the pore already made of very small grains, and subsequent condensation on the other side of the pore. The examination of the morphology of the inner surface of a pore has been carried out. The size of the grains visible was measured and three families of grain sizes were detected (see Fig. 13d, which was taken on a HBS sample of 96 MWd/kgHM) and a fractal dimension of 2.3 calculated[1].

At much higher burn up this process could lead to ultimate pores formation shown in Fig. 13c. This pore is perfectly circular, and surrounded by an amorphous looking crown itself limited by other small ultimate pores in formation. This type of pores survives the annealing process up to above 1500 K. Figs. 13e and f show similar ultimate pores, found on the small particles after loss of integrity of the sample after temperature annealing.

5.3. Mo–Ru–Tc–Pd–Rh alloy particles

Fig. 14 shows examples of the five metal particles located in pores after annealing at different temperatures. Table 3 summarizes the results of the EDX analysis of Mo, Tc, Ru, Rh and Pd in these particles in, or near, normal and ultimate pores at different annealing temperatures. Table 3 also shows the calculated average composition of these metals in the precipitates, assuming that ^{239}Pu was the only fissile element [27]. It can be clearly seen that Mo shows a deficit in the metallic particles, and on the contrary, that Tc seems to be in excess. The deficit or excess of Mo in the metallic particles (normalised to the calculated value) at different positions and at different annealing temperatures are represented graphically in Fig. 15. The Mo concentration in particles presents a significant deficit in the normal pores (NP) whereas it is close to the calculated value for ultimate pores (UP).

[1] The fractal dimension, *d*, of the structure was calculated using the following equation: $d = \log p / \log q$ where *p* is the number of fractals and *q* is the magnification. A fractal dimension of 2.3 is found which is very close to the average fractal dimension of a cauliflower (2.3) which is the structure of which the high burn-up fuel was referred after the first observations.

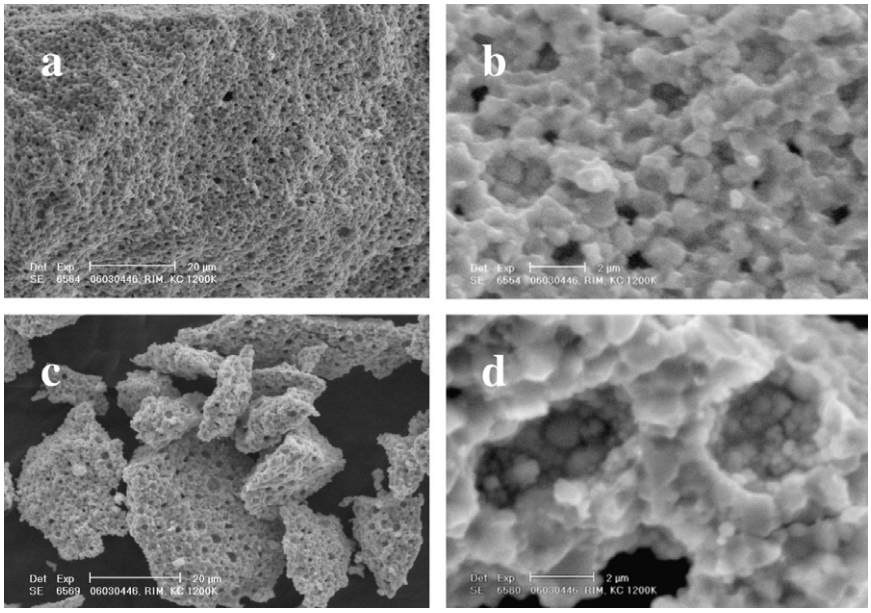

Fig. 9. Microstructure of the fuel after annealing at 920 K. The SEM micrographs (a) and (b) were recorded on area Z_b and the micrographs (c) and (d) on area Z_a (cf. Fig. 1).

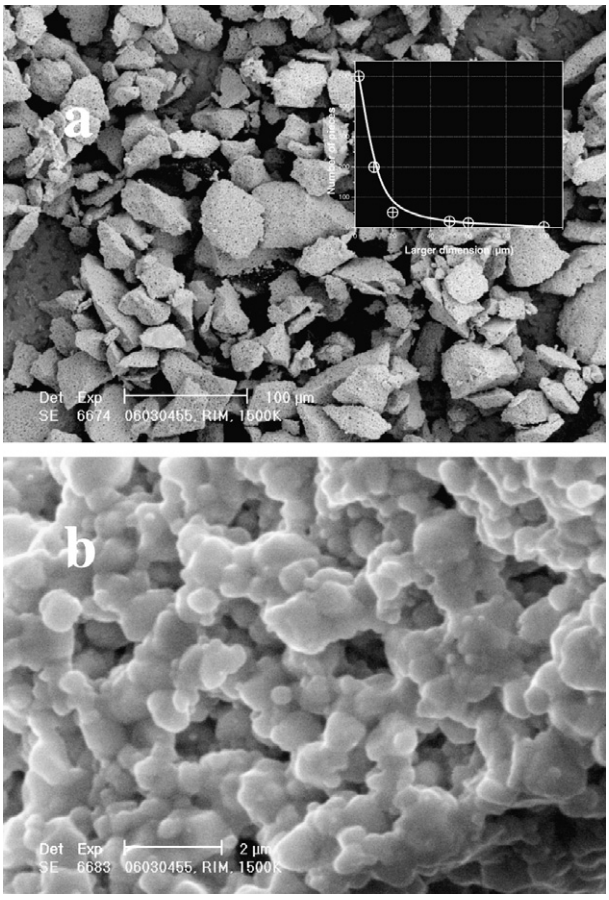

Fig. 10. SEM micrograph showing (a) an overview of the sample annealed at 1500 K and (b) a higher magnification SEM picture revealing a beginning of re-sintering of the material. The inset in micrograph (a) represents a statistical distribution of the particle sizes from the powdered specimen.

The other particularity of Mo concerns the position of the particles in the fuel, in normal (NP) or ultimate (UP) pores (Fig. 14). The concentration near ultimate pores is ~25% higher than near normal pores. The ultimate pores are found in the highest burn up regions, where the fissions are essentially originating from plutonium, but the Mo production should be smaller in that case. This result is also in contradiction with the evolution of the ΔG_{O_2} and the fact that this oxidation affects more Mo than the other metals of the precipitate as shown in a previous paper [28]. The only explanation could be the presence of a very stable phase around these pores (observed up to $T > 1800$ K), which could reduce locally on a microscopic scale the ΔG_{O_2}.

6. Discussion

6.1. Microstructural changes

The general structure of the sample changed with annealing temperature. A loss of integrity was observed which was related to the local burn-up and/or the pore size. During the heating of the sample, the pressure in the pores (increasing up to 5 times from room temperature to 1500 K), is most likely the cause of the sample pulverisation at 920 and 1500 K. Fig. 10 shows that at 1500 K more and more interconnection and/or size reduction occurs, as well as re-sintering of micro-crystals. At 1800 K the mean size of crystals, originally between 0.2 and 0.5 μm, increased to 2–4 μm.

Also a change of the pore morphology was observed, resulting in a peculiar type of pore in the highest burn-up region of the sample, which we called 'ultimate pores', as shown in Figs. 12 and 13. This type of pore is the observable limit of the cauliflower fractal structure visible in pores formed in the HBS (Fig. 13(d)), most likely formed by sputtering of pore's surface materials by fission spikes. These pores have a perfect spherical symmetry, have a dense rim of a glassy looking material and remain unchanged when heated to temperatures higher than 1500 K. Smaller pores of this type develop around the 'mother pore' and the material around them looks amorphous.

6.2. Release processes of fission gases and helium

As described in Section 4, the release of fission gases occurs in four steps at about 600, 1000, 1500 K and between 1600 and 2800 K (Fig. 3). For helium only the first three steps have been

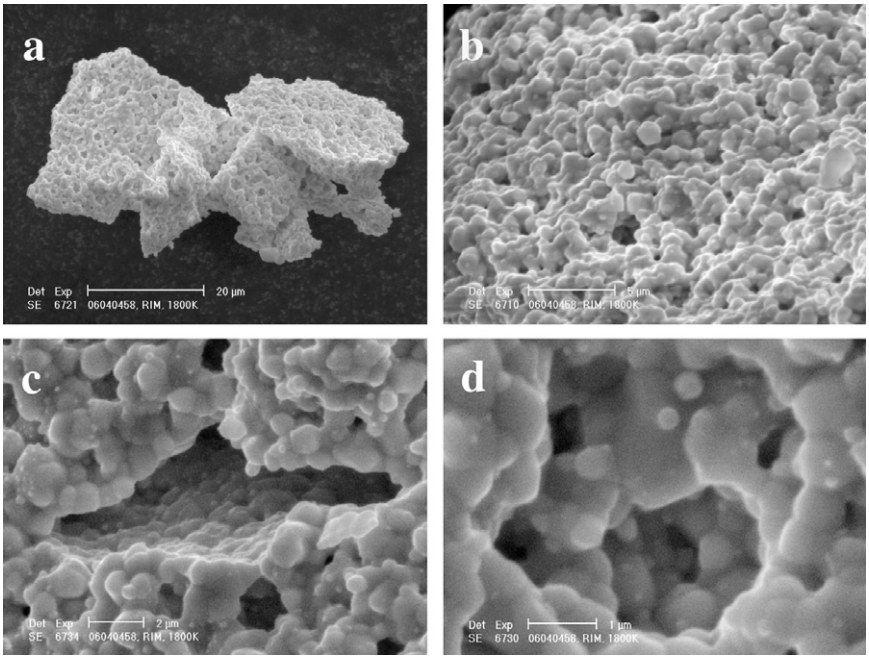

Fig. 11. SEM micrographs showing (a) the particle structure, (b) a more detailed surface microstructure (c) the structure of a cavity and (d) the structure inside a pore of a sample annealed at 1800 K. Some metallic precipitates are visible in micrograph (d).

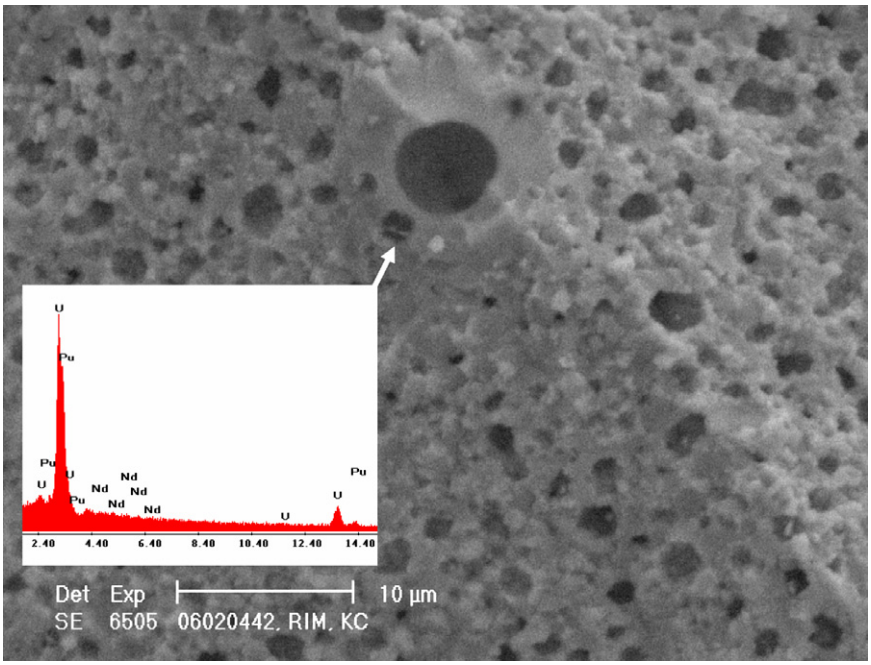

Fig. 12. SEM micrograph of the zone Z_a showing different types of pores, and the so-called ultimate pore. The EDX analysis (the spectrum is inset) of the 'amorphous' phase around the ultimate pore indicates it is mainly composed of U and Pu.

observed. These releases are continuous processes except the main steps at 1000 and 1500 K, (the small release observed at 1200 K is similar to the other) which are characterised by explosive gas release evident from the pressure transients observed on the vacuum gauges (Fig. 6). These pressure spikes are explained by burst releases of the gas contained in closed pores. The origin of this phenomenon is supported by the microscopic observation of the sample annealed at 900 and 1500 K, where a stepwise loss of integrity of the sample was observed (Fig. 9 for 900 K and Fig. 10 for 1500 K). These observations are a direct proof of the origin of the released fission gases and helium, which are localized mainly in pores. The release observed at 900 K is mainly related to the region Z_a ($0.96 < r/r_o < 1$) and the release at 1500 K to the region Z_b ($0.91 < r/r_o < 0.99$) of the sample. This suggests that Z_a, which has larger pores, is more fragile than Z_b. Our observations do not exclude that some gas (10–20%) remains in the grains and is released through a bulk diffusion mechanism in this temperature range.

The EFFUS calculations showed that the release process enthalpies ΔH_I (corresponding to Z_a) and ΔH_{II} (corresponding to Z_b) are quite close for the He, Kr and Xe (Table 2), indicating that the

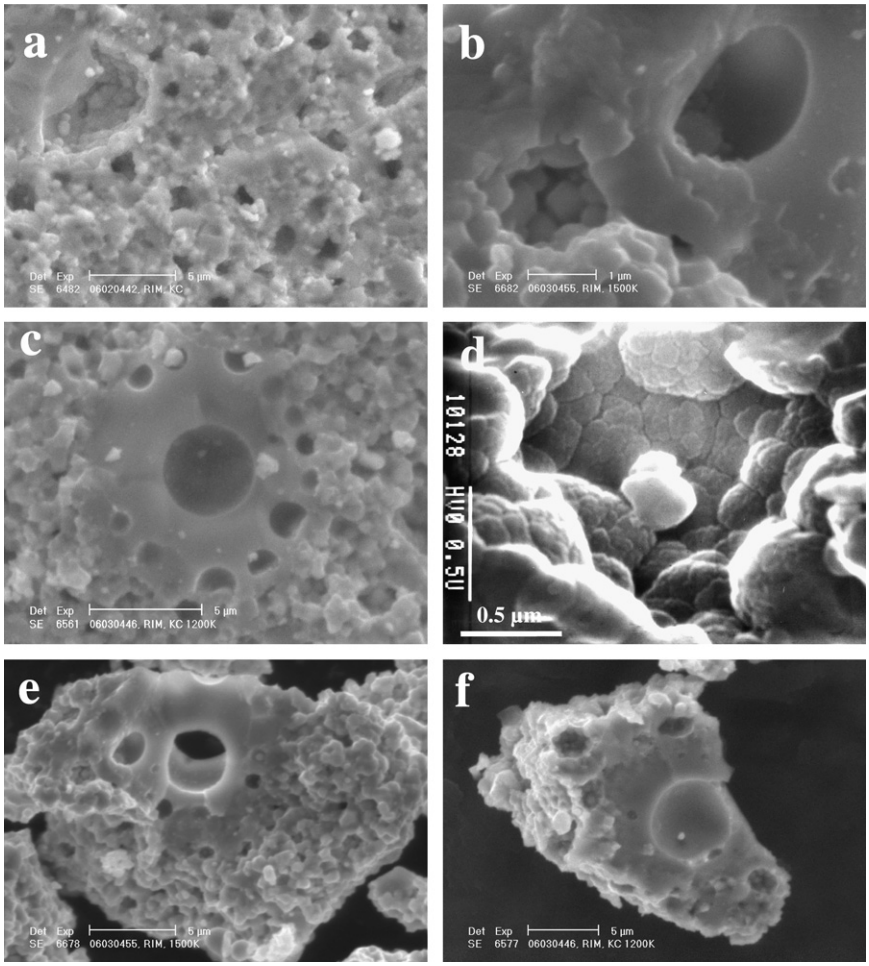

Fig. 13. SEM micrographs (a), (b), and (c) show the evolution of pores from 'normal' to 'ultimate', Micrograph d highlights the genesis of an ultimate pore in the rim region with a burn up between 140 and 260 MWd/KgHM, micrographs e and f show parts of ultimate pores after loss of integrity of the sample above 1500 K.

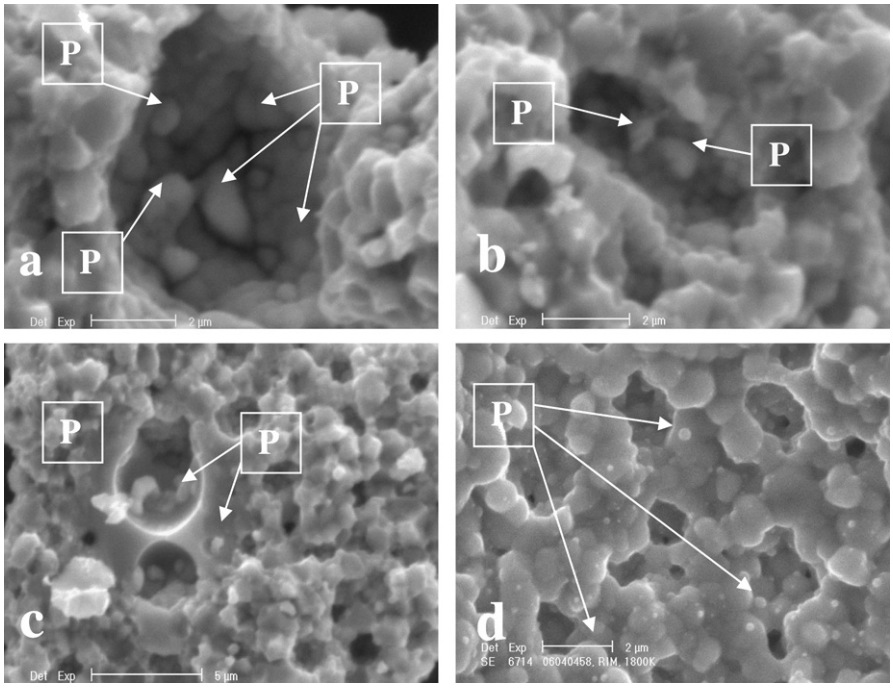

Fig. 14. Metallic particles observed in normal pores after annealing at 920 K (micrographs. a and b) in ultimate pores (micrograph c) and after annealing at 1800 K (micrograph d).

Table 3
Concentration of Mo, Tc, Ru, Rh, Pd in metallic particles, of the rim sample at different positions and at three annealing temperatures (920, 1500 and 1800 K)

	No. of particles examined	Annealing Temp. (K)	Elements (wt%)				
			Mo	Tc	Ru	Rh	Pd
Calculated composition[a]			26	9	33	9	23
Particles in normal pores	16	920	15.9 ± 1.2	14.6 ± 1.1	32.6 ± 0.9	10.9 ± 0.8	25.9 ± 1.4
Particles in ultimate pores	6	920	25.2 ± 1.5	12.1 ± 0.6	30.1 ± 1.6	9.5 ± 1.2	23.1 ± 2.0
Particles in normal pores	3	1500	20.0 ± 1.0	15.5 ± 2.0	31.7 ± 1.8	8.2 ± 0.9	23.6 ± 0.9
Particles in ultimate pores	2	1500	28.6 ± 2.1	14.2 ± 2.5	30.6 ± 1.7	8.1 ± 1.0	18.5 ± 1.1
Particles in normal pores	4	1800	12.1 ± 2.1	18.75 ± 3.0	37.6 ± 1.4	10.2 ± 1.2	17.4 ± 1.8

The first row indicates the mean quantities of these metals produced during irradiation [8]. It is assumed that these elements are not soluble in the UO_2 matrix and all precipitate into particles.
[a] calculated with the assumption that ^{239}Pu is the only fissile isotope [27].

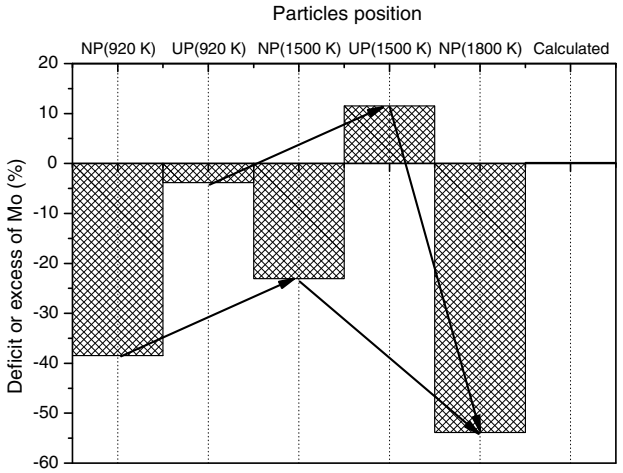

Fig. 15. Deficit or excess of Mo in metallic particles in normal (NP) and ultimate (UP) pores, after annealing at 920 K, 1500 K and 1800 K.

release mechanisms at 920 K and 1500 K are similar. Probably the overall process is a combination of two mechanisms: intra-granular diffusion of gas from the pores to the free surface, and an explosive release due to gas freed from pores close to fracture surfaces during the pulverisation of the sample.

If we consider a uniform porosity (around 25%) in the sample [29], and less but larger pores in Z_a compared with Z_b, it can be concluded from the gas release measurement that the gas pressure is equal in large and small pores. If one then considers that the total volume of $Z_a = Z_b/3$ (Fig. 1), a factor of 3 in the gas release would be expected, which is indeed observed in the measurement (Fig. 7). For example, for Xe, FR_{Za} ($T < 900$) = FR_{Zb} ($900 < T < 1500$)/3, where FR is the fractional release. The remainder of the gas (<10%) is probably dissolved or precipitated in intra-granular nano-bubbles, and corresponds to the quantity detected by EPMA [4].

In addition to these two main release steps, 1% release occurs at low temperature between 500 and 700 K. It involves the gas precipitated at the grain boundaries. Finally close to 5% release occurs at high temperature (between 1600 and 2800 K), continuing until vaporization of the sample is complete. This fraction concerns the fission gas precipitated in intragranular bubbles. The presence of a small quantity of intragranular bubbles has been confirmed by TEM observation of high burn-up samples [14].

The measured quantities of Kr and Xe in the sample are 1.02×10^{-5} and 3.41×10^{-4} mol/(g fuel), respectively, corresponding to (4.5 ± 2.3) wt% Xe in the fuel. The quantity of He deduced from the mass spectrometric signals is 6.5×10^{-6} mol/(g fuel). It is not straightforward to compare the Xe concentration detected in the fuel with the amount of Xe produced. The latter value can be approximated as about 3.0 wt% Xe in the fuel, calculated from the fission yield of ^{239}Pu and the burn-up. This value is in fair agreement with the measured value, implying that the major part of the xenon produced is still present in the rim.

The measured Xe/Kr ratio is very large (33). The Xe/Kr ratio derived from literature is 5.9 for ^{235}U fission, whereas the same ratio is 15 for ^{239}Pu fission and 17 for ^{241}Pu fission [30]. The evolution of the Xe/Kr ratio with the burn-up is given in Fig. 16, comparing the present result with values measured previously on UO_2 and MOX fuels of different burn-up, most of which were obtained by Knudsen cell mass spectrometer experiments at ITU. The Xe/Kr ratio remains around 6 over a large burn-up range for highly enriched UO_2 fuel, and around 15 with a tendency to increase for MOX fuel, whereas it is low for low enriched UO_2 fuel. The present result, which seems to be consistent with the trend, might be partially due to a large contribution of fissions from higher mass actinides, ^{241}Pu, ^{242m}Am and ^{243}Cm [31], which have different fission yields. A relatively large amount of these isotopes has been measured in the vapour at high temperature. Possibly also transmutation effects (destruction of Kr, production of Xe) could play a role at such high burn-up; large amount of actinides isotopes, up to 244, were detected during the total vaporisation of this sample, subject treated in a coming article.

The total quantity of gas in the sample was 3.75×10^{-4} mol/(g fuel). This gas was mainly accumulated in pores. Since at such burn-up the closed porosity fraction increases to 25% [29,32], and taking a mean density of the sample of 10 g/cm^3, the gas pressure in the pores is calculated to be (30 ± 2) MPa (300 bar) at room temperature. This pressure increases to 90 and 150 MPa (900 and 1500 bar) at 920 and 1500 K, respectively. This pressure (given

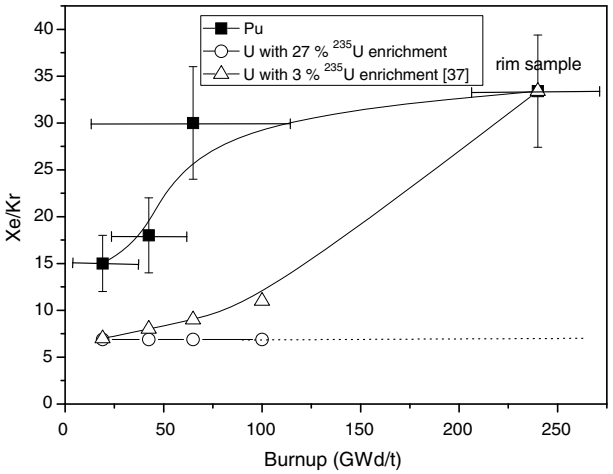

Fig. 16. Evolution of the Xe/Kr ratio as a function of the burn-up for plutonium (MOX) and uranium fuels (enrichment 3% and 27%). Our rim sample is considered as a pure plutonium fuel (all measurements perform at ITU). The triangles (Δ). are puncture results [37].

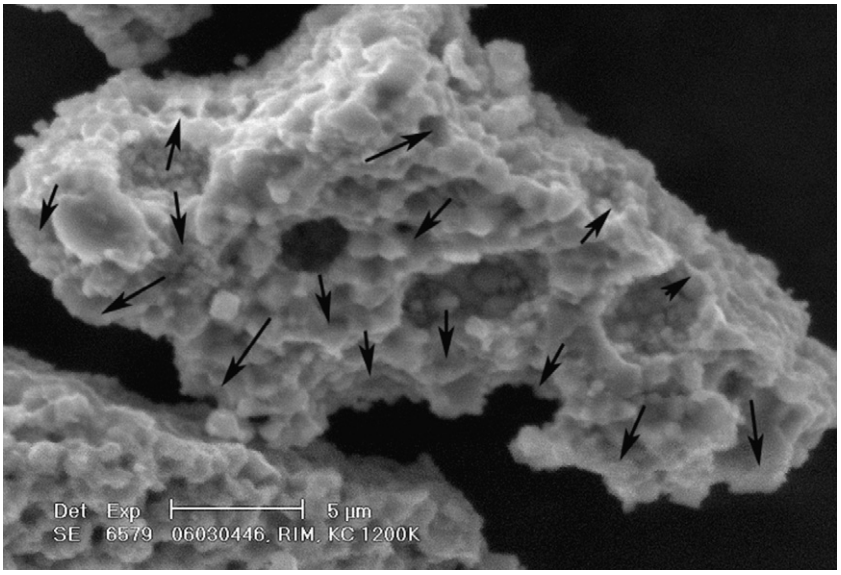

Fig. 17. SEM micrograph of a sample particle after annealing at 920 K. The arrows indicate fractured areas on pore edges.

with an uncertainty of 50%) is of the same order as the pressure calculated in [33,34]. The pressure achieved seems to be sufficient to produce the rupture of the grains along the original grain boundaries. The micro-cracking as such, related to porosity and fracture stress, was probably not the cause of the pulverisation of the material at higher temperature but rather embrittlement on pore edges at the grain boundaries (Fig. 17).

6.3. Release processes of volatile fission products

The release of the most volatile fission products (Cs, Rb, I, Te) (Fig. 4) follows the release of the fission gases to some extent, which indicates that they are also localized mainly in pores and in the rim around the pores. The diameter of the entity pore-rim is about 10 μm, corresponding to the length of a fission fragment track. Fig. 7 shows the pore structure before and after annealing at 920 K. The rim that is under formation around the pore disappears after annealing. It is expected to contain 25% of these fission products. At this stage of formation the entity pore-rim is still thermally sensitive. The chemical nature of these elements is difficult to determine, but taking into account the relatively large ΔG_{O_2} of the sample and the results presented in a previous paper [29], Cs could form compounds like CsI, but also more complex ones with Zr, Mo or Te.

Barium and Strontium vaporise smoothly and are detected successively at 1500 and 1800 K and reach maxima at 2000 and 2400 K. The vaporisation enthalpies measured between 1500 and 2000 K for Ba and between 1800 and 2300 K for Sr are 354.1 kJ/mol and 321.6 kJ/mol, respectively. For comparison, the vaporisation enthalpies of BaO and Ba from the pure oxide are 413 and 158 kJ/mol, the $\Delta H_{vap}$of SrO and Sr being 511 and 158 kJ/mole [19,35]. Barium has been detected in a secondary phase rich in Zr, U, Pu, as shown in Fig. 4, the so called grey phase [24]. Strontium is considered as highly soluble in the UO_2 matrix [36], most likely as SrO, but is detected only as Sr by mass spectrometry. The vaporisation of Sr occurs earlier than the vaporisation of lanthanides which will be subject of another paper.

6.4. The noble metals

Molybdenum, Ru, Tc, Rh and Pd were not detected in the fuel by mass spectrometry except MoO, but were found in the five metals particles precipitated after annealing at 920, 1500, 1800 K in or around pores (Figs. 10–13). The Mo concentration in the particles showed a significant deficit in the normal pores (NP) whereas it was close to the calculated value for ultimate pores (UP). This deficit can be due to the fact that the sample has a relatively high ΔG_{O_2} which could favour the formation of phases containing oxidised Mo (e.g. Cs_2MoO_4). It is not expected that Mo is in solution in the UO_2 matrix, because of his poor solubility [36]. With increasing temperature and local fluctuations of the oxygen potential this phase could be reduced, producing Cs that is released and Mo that diffuses into the metallic particles. At temperatures higher than 1500 K the Mo concentration decrease could be attributed to a reverse mechanism. Mo is released as MoO_3 due to the increase of oxygen potential of the fuel with temperature [28]. The monoxide of Mo was indeed detected as ^{95}MoO, ^{98}MoO, ^{100}MoO between 1450 and 1600 K whereas the dioxide was masked by iodine and xenon, and the masses corresponding to molybdenum trioxide were not measured below 1800 K. At higher temperature the MoO_3 masses correspond to the lanthanide metals vaporising from the sample, masking eventual MoO_3 signals. The signals for metallic molybdenum were too low. The fact that Mo was detected as oxide at the same temperature as Cs, Rb, I, and Te could indicate its participation in complex phases containing these elements at the pores surface, as shown in Fig. 7.

7. Conclusions

The results of the mass spectrometric and microscopic studies of a HBS sample from the periphery of high burn-up UO_2 fuel pellet (average burn-up of 200 ± 20 MWd/KgHM) show that the release of fission products is also related to changes in the microstructure of the sample. The microstructure was not observed to influence release at low burn-up [16]. The measured absolute amount of Xe suggests that a major part of the fission gas produced is still present in the HBS. This means that the pressure in the pores of the HBS structures can reach values up to 30 MPa, causing the rupture of the grains along the original grain boundaries. This process is accompanied by explosive gas releases (at 1000 and 1500 K) that are superposed on a continuous release process. With increase in temperature the typical HBS microstructure changes to form larger grains and interconnected pores. Large symmetrical pores

surrounded by an amorphous phase: so-called 'ultimate pores' were detected and found to be stable up to 1800 K. Further studies on the HBS in the Pu-rich particles of MOX should provide further information about the relevance of these finding during irradiation.

References

[1] J. Belle, Naval Reactors Handbooks, United States Atomic Energy Commission, 1961.
[2] R. Manzel, C.T. Walker, J. Nucl. Mater. 301 (2002) 170.
[3] H. Matzke, J. Spino, J. Nucl. Mater. 248 (1997) 170.
[4] M. Mogensen, C. Bagger, C.T. Walker, J. Nucl. Mater. 199 (1993) 85.
[5] M. Mogensen, J.H. Pearce, C.T. Walker, J. Nucl. Mater. 264 (1999) 99.
[6] J. Spino, D. Baron, M. Coquerelle, A.D. Stalios, J. Nucl. Mater. 256 (1998) 189.
[7] J. Spino, D. Papaioannou, J. Nucl. Mater. 281 (2000) 146.
[8] J. Spino, J. Rest, W. Goll, C.T. Walker, J. Nucl. Mater. 346 (2005) 131.
[9] C.T. Walker, V.V. Rondinella, D. Papaioannou, S.V. Winckel, W. Goll, R. Manzel, J. Nucl. Mater. 345 (2005) 192.
[10] C.T. Walker, D. Staicu, M. Sheindlin, D. Papaioannou, W. Goll, F. Sontheimer, J. Nucl. Mater. 350 (2006) 19.
[11] D. Baron, J. Spino, Technical Commitee Meeting on Technical and Economical Limits to Fuel Burnup Extension, IAEA, San Carlos de Bariloche, Argentina, 1999.
[12] D. Baron, International Workshop on the High Burn-up Structure in Nuclear Fuels ITU Karlsruhe, Germany, 2004.
[13] M. Kinoshita, T. Sonoda, S. Kitajima, A. Sasahara, T. Kameyama, T. Matsumura, E. Kolstad, V.V. Rondinella, C. Ronchi, J-P. Hiernaut, T. Wiss, F. Kinnart, J. Ejton, D. Papaioannou, H. Matzke, in: Proceedings of the International meeting on LWR Fuel Performance, Orlando, Florida, 2004.
[14] T. Sonoda, M. Kinoshita, I.L.F. Ray, T. Wiss, H. Thiele, D. Pellottiero, V.V. Rondinella, H. Matzke, Nucl. Instrum. Meth. B 191 (2002) 622.
[15] C. Ronchi, M. Sheindlin, D. Staicu, M. Kinoshita, J. Nucl. Mater. 327 (2004) 58.
[16] F. Capone, J.P. Hiernaut, M. Martellenghi, C. Ronchi, Nucl. Sci. Eng. 124 (1996) 436.
[17] F. Capone, J.Y. Colle, J.P. Hiernaut, C. Ronchi, J. Phys. Chem. A 103 (1999) 10899.
[18] J.Y. Colle, J.-P. Hiernaut, D. Papaioannou, C. Ronchi, A. Sasahara, J. Nucl. Mater. 348 (2006) 229.
[19] R. Hultgren, R.L. Orr, P.D. Anderson, K.K. Kelley, Selected Values of Thermodynamic Properties of Metals and Alloys, John Wiley, Inc., New York, 1963. p. 30.
[20] J. Mann, J. Chem. Phys. 46 (1967) 1646.
[21] J.W. Otvos, D.P. Stevenson, J. Amer. Chem. Soc. 8 (1956) 546.
[22] R. Grimley, in: J.L. Margrave (Ed.), The Characterisation of High Temperature Vapors, John Wiley, NY, 1967.
[23] C. Ronchi, J.P. Hiernaut, J. Nucl. Mater. 325 (2004) 1.
[24] H. Kleykamp, J. Nucl. Mater. 131 (1985) 221.
[25] J.P. Hiernaut, C. Ronchi, J. Nucl. Mater. 294 (2001) 39.
[26] Masumichi Koizumi, Masakazu Satoh, Kenji Noro, J. Nucl. Mater. 51 (1974) 90.
[27] B.R.T. Frost (Ed.), Materials Science and Technology, Verlagsgesellschaft GmbH, 1994.
[28] J.P. Hiernaut, T.A.G. Wiss, D. Papaioannou, J.R.M. Konings, V.V. Rondinella, J. Nucl. Mater. 372 (2008) 215.
[29] J. Spino, A.D. Stalios, H. Santa Cruz, D. Baron, J. Nucl. Mater. 354 (2006) 66.
[30] M. Mogensen, Int. J. Mass Spectrom. 48 (1983) 389.
[31] H. Gruppelaar, J.L. Kloosterman, J.R.M. Konings, Advance Technologies for the reduction of Nuclear Waste, Netherlands Energy Research Fundation ECN, 1998.
[32] J. Spino, D. Papaioannou, J.-P. Glatz, J. Nucl. Mater. 328 (2004) 67.
[33] Y.-H. Koo, B.-H. Lee, J.-S. Cheon, D.-S. Sohn, J. Nucl. Mater. 295 (2001) 213.
[34] J. Spino, K. Vennix, M. Coquerelle, J. Nucl. Mater. 231 (1996) 179.
[35] L.V. Gurvich, V.S. Iorich, D.V. Chekhovskioi, V.S. Yungman, IVTANTHERMO, CRC, Boca Raton, FL, 1993.
[36] H. Kleykamp, J. Nucl. Mater. 206 (1993) 82.
[37] S. Bremier, R. Manzel, C.T. Walker, in: Proceedings of OECD/AEN/NEA Inter.Seminar on Fission Gas Behaviour in Water Reactors, CEN, Cadarache, France, 26–29 September 2000.